Supplementary Material

Flexible Polarization Rotation at Ferroelectric-Metal Interface as Seed for Domain Nucleation

Xian-Kui Wei,[1,2*] Yurong Yang,[3] Leo J. McGilly,[1] Ludwig Feigl,[1,4] Rafal E. Dunin-Borkowski,[1] Chun-Lin Jia,[2,5] Laurent Bellaiche,[3*] and Nava Setter[1,6]

[1]*Ceramics Laboratory, EPFL-Swiss Federal Institute of Technology, Lausanne 1015, Switzerland*

[2]*Ernst Ruska-Centre for Microscopy and Spectroscopy with Electrons and Peter Grünberg Institute, Forschungszentrum Jülich GmbH, 52425 Jülich, Germany*

[3]*Physics Department and Institute for Nanoscience and Engineering, University of Arkansas, Fayetteville 72701, USA*

[4]*Institute for Photon Science and Synchrotron Radiation, KIT - Karlsruhe Institute of Technology, Hermann-von-Helmholtz-Platz 1,76344 Eggenstein-Leopoldshafen, Germany*

[5]*School of Microelectronics, Xi'an Jiaotong University, Xi'an 710049, China*

[6]*Department of Materials Science and Engineering, Tel-Aviv University, Ramat Aviv 69978, Israel*

I. Experimental methods

1. Thin film growth and lamella specimen preparation

The $Pb(Zr_{1-x}Ti_x)O_3$ (PZT, x = 0.9, 0.6) and $BiFeO_3$ thin films were grown by pulsed laser deposition on $SrRuO_3$-buffered (110)-plane $DyScO_3$ and (001)-plane $SrTiO_3$ substrates (CrysTec GmbH) [31,32]. Lattice parameter relationships show that the (x = 0.9) PZT films are subject to a weak tensile strain (~ 0.9%) from the $DyScO_3$ substrate, with the mismatch strain balanced by formation of the ferroelastic *c/a/c/a* domain array over the entire film [29]. As a result of a compressive strain of ~ -2.3% from the $SrTiO_3$ substrate, the x = 0.6 PZT film forms a monodomain ferroelectric state. On the $DyScO_3$ substrate, the $BiFeO_3$ film has a compressive

strain of ~ -0.4% and forms a regular 71° domain array, which is associated with presence of complex nanodomains near the surface, interface and 71° DWs. A focused ion beam system (FEI Helios NanoLab 400S) was used for lamella specimen preparation for (scanning) transmission electron microscopy ((S)TEM) studies. For preparation of the electric-field biased specimens, an additional Pt electrode with a thickness of > 2 μm was deposited on the PFM-written domain array for protection of the written domain boundaries. A lower voltage and beam current were used to reduce Ga-ion beam damage during thinning of the lamella. A NanoMill 1040 system was used to remove surface contamination and to reduce the specimen thickness.

2. Quantitative atomically-resolved (S)TEM and dark-field imaging

The atomically-resolved (S)TEM investigations were performed on an image-corrected FEI Titan 80-300 microscope operated at 300 kV and a probe-corrected FEI Titan 80-200 ChemiSTEM microscope operated at 200 kV. Quantitative measurements of atomic column positions were carried out by fitting the column intensities with two-dimensional Gaussian peaks on the basis of maximum likelihood estimation. Structure modelling and image simulation were carried out using CrystalKit-MacTempas software package. For quantitative TEM study, an iterative procedure for comparison of the experimental image with the simulated ones was performed to unravel the effects of specimen tilting away from the Laue orientation, residual lens aberrations and interfacial element diffusion on the image contrast. The effective charges of $PbTiO_3$, with Z^*_{Pb} = 3.92, Z^*_{Ti} = 6.71, Z^*_{O1} = -5.51 and Z^*_{O2} = -2.56, were used for calculating the spontaneous polarization based on the formula $P_S = \frac{1}{V}\sum_i \delta_i Z_i^*$ [33]. Dark-field imaging was carried out on FEI Tecnai F20 and FEI Titan 80-300 microscopes.

3. Quantitative compositional analysis across the PZT/$SrRuO_3$ interfaces

A probe-corrected FEI Titan 80-200 Chemi-STEM microscope equipped with a high-brightness Schottky field emission electron gun and a Super-X energy-dispersive X-ray spectroscopy (EDS) system was used to carry out the quantitative compositional analysis. For the investigated interfaces, the EDS signal collected from different interface areas yields the consistent results. Comparison of the SrO-Zr/TiO_2 terminated interfaces shows that the interfacial mismatch strain may influence the composition diffusion. Particularly, the diffusion of Sr into the PZT layer becomes less evident in compressive-strained film than the tensile-strained films. Apart from the EDS, the atom-column intensities, which are dependent on the atomic numbers [34], are extracted from the experimental images to identify the atomic termination planes at the interfaces.

4. First-principles calculations of Sr and Ru co-doped $PbTiO_3$ supercells

Calculations of Sr and Ru co-doped $PbTiO_3$ were performed using density-functional theory, as implemented in the Vienna *ab initio* simulation package [35]. An energy cutoff of 550 eV was used, and projector-augmented wave potentials [36] were employed to describe the electron-ion interactions. Figure 2(c) shows that the second to fourth polarization points in domain II (counting from the interface), which correspond to 3 unit cells (approximately 1.2 nm) from the $SrRuO_3$/domain II interface, are particularly interesting points. Figure 3(f) shows that, in this local area, the stoichiometry of both Pb and Ti is close to 75% and that of Sr is close to 25%. Therefore, supercells of $(Pb_{0.75}Sr_{0.25})(Ti_{0.75}Ru_{0.25})O_3$ containing 40 atoms were used as approximate models to calculate the polarization behavior in domain II. Ferromagnetic coupling between Ru atoms was also considered. Electronic relaxations converged within 10^{-6} eV and ionic relaxation was performed until the residual force on each ion was less than 0.002 meV/Å. The PBE+U functional (with U = 2.5 eV, J = 0.4 for the Ru ions) was used [37]. Polarization was

calculated by computing the product between Born effective charges and atomic displacements. The lattice constants of bulk $SrRuO_3$ are a = 5.582 Å, b = 5.629 Å, c = 7.895 Å. The thin films of $(Pb_{0.75}Sr_{0.25})(Ti_{0.75}Ru_{0.25})O_3$ were calculated by fixing the in-plane lattice constant to be 3.97 Å, according to the lattice constants of bulk $SrRuO_3$.

5. *Ex-situ* electric-field biasing and electron microscopy experiments

An FEI Nova 600 Dualbeam system was used to fabricate Pt electrodes through electron-beam induced deposition (EBID). In this process, the chamber was evacuated to a base pressure of approximately 1×10^{-6} mbar. A precursor gas of $(CH_3)_3CH_3C_5H_4Pt$ was introduced and dissociated in the presence of a focused electron beam, leading to locally deposited Pt in patterns that were defined by raster scanning of the beam. The accelerating voltage was 5 kV and the beam current was 1.6 nA. An Asylum Research atomic force microscope operating in piezoresponse force microscopy (PFM) mode was then used to image and address the EBID Pt electrodes. ASYELEC-01 Ti/Ir coated Si probes with a force constant of ~3 N/m were used to image the domain states and to switch the polarization direction. Voltage pulses of +8 V for a duration of >1 s were used to switch the polarization from an "upward" orientation (towards the free surface) to a "downward" orientation (towards the substrate).

II. Supplementary text

1. Domain polarization and interface features in (x = 0.9) PZT/$SrRuO_3$/$DyScO_3$ films

In (x = 0.9) PZT/$SrRuO_3$/$DyScO_3$ thin films, the tensile substrate strain (~ 0.9%) leads to the formation of a ferroelastic *c/a/c/a* domain array. As illustrated in Fig. S1(a), in thinner films ($t \leq 80$ nm) the substrate strain is maintained in the *c* domains, leading to a larger *c/a* ratio of the *a* domains than the *c* domains. This is manifested by a parallelogram shape of the ferroelastic *a*

domains [Figs. S1(b)-S1(d)]. In thicker films ($t > 80$ nm), strain release results in a larger *c/a* ratio for *c* domains than *a* domains, resulting in the formation of V-shaped *a* domains [see Fig. S5]. Details about film-thickness-regulated strain release and domain wall (DW) feature changes are discussed elsewhere [29]. In our experiments, dislocations are rarely (or almost never) observed near the DWs and interfaces. Through systematic (S)TEM investigations, we found that ferroelectric *c* domains in the $DyScO_3$-substrated PZT films exhibit the following features. (1) In the thinner films, the *c* domains tend to split into two domains by the negatively charged interfacial CDW, as shown in Fig. 1c, domain I (the major part) with an upward P_S orientation towards the surface and domain II (the minor part) with a downward P_S orientation towards the interface [Figs. 1c, S1(e), S1(f)]. In the thicker films, the entire *c* domains adopt a downward P_S orientation [Fig. S5]. (2) In the thinner films, the PZT/$SrRuO_3$ interface is essentially terminated by the SrO-Zr/TiO_2 atomic planes [Figs. 3, S2], as further manifested by atom-column intensity profiles shown in Fig. S1(g). While in the thicker films, the PZT/$SrRuO_3$ interface is essentially terminated by RuO_2-PbO atomic planes [Figs. S5, S7]. (3) Irrelevant to types of the termination planes, either SrO-Zr/TiO_2, RuO_2-PbO or Au-PbO, the structural and chemical reconstruction always leads to a monoclinic lattice distortion, which is featured by flexible polarization rotation at the ferroelectric-metal interfaces [Figs. 1d, S1(f), S5-S9].

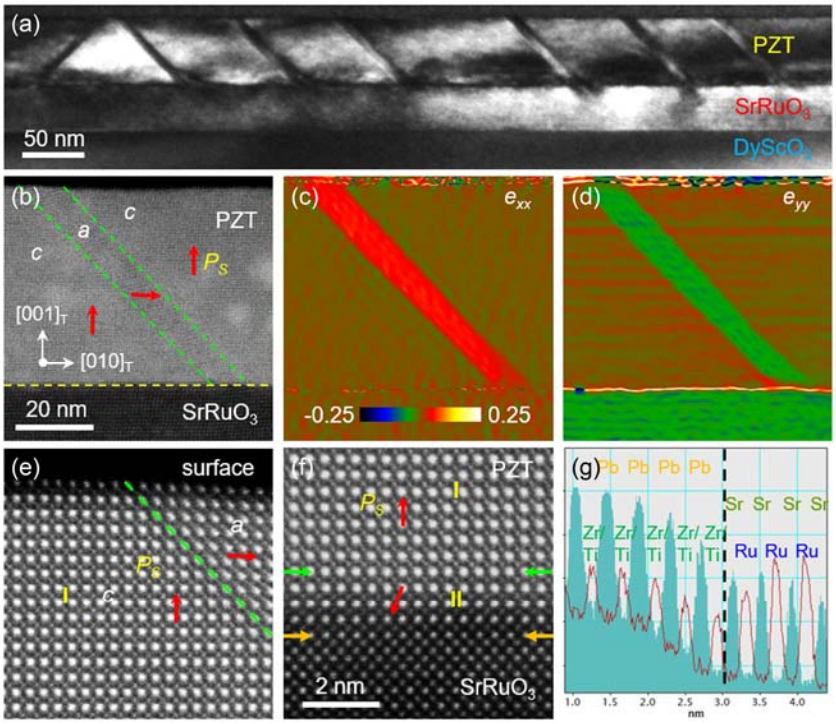

FIG. S1. (a) Cross-sectional bright-field TEM image of a 45-nm-thick (x = 0.9) PZT/$SrRuO_3$/$DyScO_3$ thin film recorded along $[100]_T$ direction. (b)-(d) HAADF-STEM image of the ferroelastic 90° domains with a head-to-tail P_S configuration, shown alongside strain maps of (c) e_{xx} and (d) e_{yy} obtained by geometrical phase analysis (GPA). The green dashed lines mark the 90° DWs. (e),(f) Atom-resolved HAADF-STEM image of *c* (and *a*) domains illustrating (e) an upward (and rightward) P_S direction for the *c* (and *a*) domains towards the surface and (f) a downward-rotated P_S direction near the interface. Orange and green arrows mark the SrO-Zr/TiO_2 terminated interface and the tail-to-tail CDW, respectively. (g) Atom-column intensity profiles of evidencing a RuO_2-SrO-Zr/TiO_2-PbO terminated interface (black dashed line).

2. Mismatch orientation between (x = 0.9) PZT layer and $SrRuO_3$ electrode

Figures S2(a) and S2(b) show the original experimental data for the relative displacements of the intensity peaks corresponding to the oxygen columns, normal to ($\delta z_{O2\text{-}B}$)

and parallel to ($\delta x_{O2\text{-}B}$) the interface respectively, measured from the experimental image shown in Fig. 1(c). Along the normal direction of the film, the mutual penetration and compromise of the antiferrodistortive order in $SrRuO_3$ with the polar order in the PZT can clearly be seen near the interface. Furthermore, the transition of oxygen displacements from one direction to the opposite direction is clearly displayed across the CDW. Along the interface direction, the evident displacements of oxygen ($\delta x_{O2\text{-}B}$) at both sides of the interface can be well identified and the null displacements ($\delta x_{O2\text{-}Zr/Ti}$) near the CDW are clearly revealed.

We note also that in the $SrRuO_3$ electrode layer the antiferrodistortive ordered oxygen columns have a net upward shift with respect to the Ru columns. This net shift is considered to be an artifact resulting from local crystal tilt from the $[010]_O$ zone axis of $SrRuO_3$. Ideally, the specimen would be flat without bending and the structural model of the interface would follow the crystallographic orientation relationship with the $[1\bar{1}0]_T$ direction of the PZT film, which is parallel to the $[010]_O$ direction of $SrRuO_3$ electrode. However, comparisons of image simulations with the experimental image show that the orientation relationship between the PZT film and the $SrRuO_3$ electrode does not follow this relationship exactly. The misorientation is confirmed by the fact that the simulated images based on the above orientation relationship do not match the experimental image simultaneously for both the PZT film and the $SrRuO_3$ electrode. When the best match is obtained for the $SrRuO_3$ part [Figs. S2(c), S2(d)], as judged by the oxygen displacements indicated by the cyan and yellow arrows in Fig. S2(c), the simulated image of the PZT part obviously differs from the corresponding part of the experimental image, as judged by the different contrast distribution surrounding the Pb columns, and *vice versa* [Figs. S2(d), S2(e)]. The misorientation between different regions on a specimen can be the result of the specimen bending and local distortion. Based on image simulations, a small tilt of the $SrRuO_3$

electrode layer by approximately 4 mrad from the $[010]_O$ zone axis of $SrRuO_3$ leads to a good match between the calculated and experimental images and also to an artificial upward displacement of the intensity peaks that correspond to oxygen columns in the $SrRuO_3$ electrode layer, as shown in Fig. S2(a). These artificial displacements have been removed in determination of the atomic positions which are shown in Fig. 2.

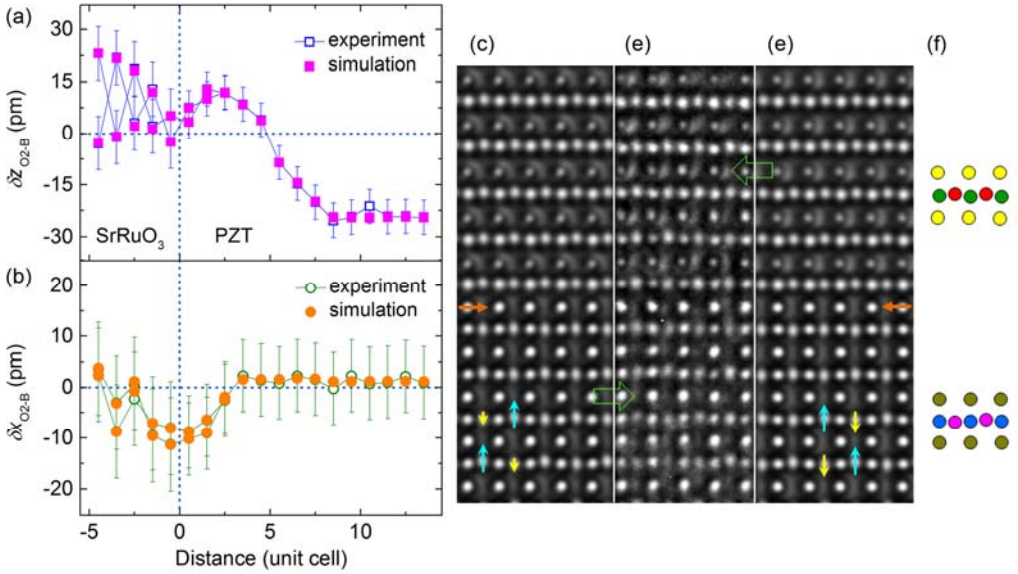

FIG. S2. (a),(b) Original experimental data (empty symbols) and simulated data (filled symbols) for the relative displacements of oxygen ($\delta z_{O2\text{-}B}$ and $\delta x_{O2\text{-}B}$) measured from the PZT/$SrRuO_3$ interface shown in Fig. 1c and its inset (t = 54 nm). (c) Simulated image of an ideal SrO-Zr/TiO_2 terminated interface (orange arrows) with tilting of the specimen by 4.0 mrad around the axis that makes a 45° angle with the interface line. (d) Averaged experimental image of the interface area. (e) Simulated image of an ideal SrO-Zr/TiO_2 terminated interface with tilting of the specimen by 3.5 mrad around the axis that makes a -5° angle with the interface line. The cyan and yellow arrows indicate vertical displacements of oxygen ($\delta z_{O2\text{-}Ru}$) inside the $SrRuO_3$ electrode. (f) Schematic crystal structure projected along the viewing direction. Atomic column

types: Pb/O1-yellow, Zr/Ti-green, O2-red in PZT; Sr/O1-dark yellow, Ru-blue, O2-pink in $SrRuO_3$.

3. Determination of the supercell used for first-principles calculations

By averaging the composition from the second to the fourth unit cells in domain II, a supercell of $(Pb_{0.75}Sr_{0.25})(Ti_{0.75}Ru_{0.25})O_3$ was constructed for first-principles calculations. During the calculations, all possible atomic configurations (corresponding to different B and A site atom orders) were constructed, including different oxygen octahedral tilting modes ($a^-a^-c^+$ and $a^0a^0c^0$), using the 40-atom supercells. The most stable structure of the supercell was found to have a monoclinic structure with space group *Cm*. From the schematic crystal structure [Fig. S3], it is seen that the Sr and Ru atoms are coordinated by six nearest-neighboring Pb and Ti atoms, respectively.

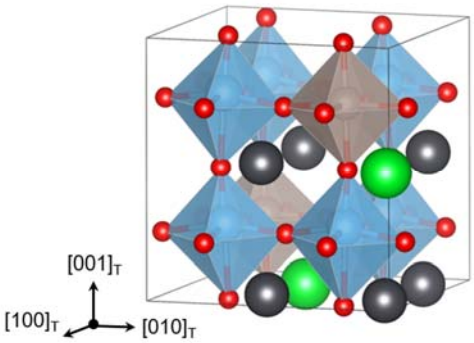

FIG. S3. 3D crystal structure of the first-principles calculated $(Pb_{0.75}Sr_{0.25})(Ti_{0.75}Ru_{0.25})O_3$ supercell with space group *Cm*. Atom types: Pb-black, Sr-green, Ti-blue, Ru-grey, O-red.

4. Effect of polar catastrophe on polarization screening at $BiFeO_3/SrRuO_3$ interfaces

For PZT (Pb^{2+}, Zr^{4+}/Ti^{4+}, O^{2-}) and $SrRuO_3$ (Sr^{2+}, Ru^{4+}, O^{2-}), uncharged AO and BO_2 atomic planes do not lead to interplanar charge transfer at their interfaces. In order to examine

the effect of polar catastrophe on polarization screening, the structure and polar displacement changes near an interface between $BiFeO_3$ (Bi^{3+}, Fe^{3+}, O^{2-}) and $SrRuO_3$ were investigated. Morphology of the $BiFeO_3$ film grown on $SrRuO_3$-electroded $DyScO_3$ substrate is shown in Fig. S4(a). Dark-field TEM imaging experiments revealed that the domains with a width of ~ 100 nm formed an inclined 71° DW array [Fig. S4(b)]. Inside the bright domains, U-shaped dark contrast was observed and the atomic-scale HAADF-STEM investigation showed that the U-shaped dark contrast arises from tail-to-tail 71° or 109° CDWs [Figs. 4, S4(c)]. Near surface of the $BiFeO_3$ film, atomic-scale STEM imaging (not shown) revealed that the tiny nanodomains (dark contrast) form a charged P_S configuration with the underlying large domain [Fig. S4(b)]. The application of geometrical phase analysis (GPA) shows that the ferroelectric $BiFeO_3$ film has grown epitaxially on the $SrRuO_3$ electrode [Fig. S4(d)], with the strain variation mainly taking place along the normal direction of the film [Fig. S4(e)], i.e., the c_p-axis changes as shown in [Fig. 4b]. Similarly, the atom-column intensity profiles clearly show that the $BiFeO_3/SrRuO_3$ interface is terminated by $SrO\text{-}FeO_2$ atomic planes [Fig. S4(f)]. Diffusion of Sr into the nearest-neighboring BiO layer can be identified, while mutual diffusion between B-site Ru and Fe appears to be limited. Therefore, the interface reconstruction, involving oxygen rotation mismatch, interfacial strain mismatch, polar catastrophe, chemical diffusion and polarization penetration, leads to a monoclinic-like lattice distortion at the $BiFeO_3/SrRuO_3$ interface, which drives the polarization to rotate flexibly within the finite space [Fig. 4]. The similar screening behavior takes place at the interfacial CDW of $BiFeO_3$.

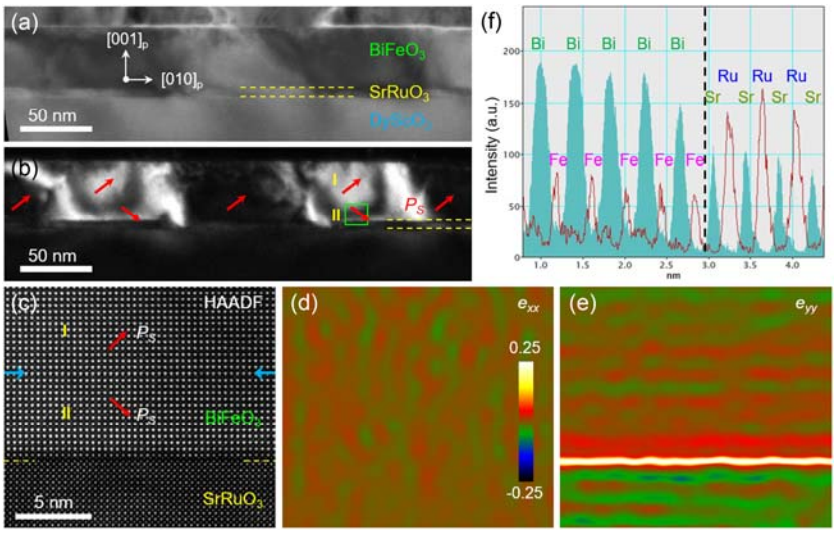

FIG. S4. (a) Cross-sectional bright-field TEM image of a (40 nm) $BiFeO_3$/(5 nm) $SrRuO_3/DyScO_3$ thin film recorded along $[100]_p$ direction. (b) Dark-field TEM image of a 71° domain array recorded using an $(002)_p$ reflection spot from domain I. The yellow dashed lines mark the $BiFeO_3/SrRuO_3$ and $SrRuO_3/DyScO_3$ interfaces. (c) HAADF-STEM image collected from the green rectangular area in (b). The blue arrows mark the tail-to-tail 71° or 109° CDW. (d),(e), Corresponding strain maps of (d) e_{xx} and (e) e_{yy} obtained by using GPA. (f) Intensity profiles of Bi-Sr and Fe-Ru columns of evidencing the RuO_2-SrO-FeO_2-BiO terminated interface (black dashed line).

5. Polarization screening at RuO_2-PbO terminated PZT/$SrRuO_3$ interfaces

Our study on (x = 0.9, 0.6) PZT and BFO films shows that, as the ferroelectric film is thin (approximately 50 nm), the ferroelectric/$SrRuO_3$ interfaces are terminated by SrO-BO_2 planes [Figs. S1(g), S4(f), S9(f)]. However, as the film thickness increases (e.g., t > 80 nm) in the DSO-substrated PZT films, the interface is essentially terminated by the RuO_2-PbO planes [Fig. S5(g)]. In comparison with the thinner films, as a result of a complex thermodynamic process during film growth [31], alternation of the interface termination is induced by film-

thickness-driven strain release [29]. This behavior is supported by the film-thickness-regulated P_S orientation in the (x = 0.9) PZT films [Figs. S1, S5] with respect to the termination-dependent screening capability of $SrRuO_3$ [52] and severe A-site elemental diffusion at the interfaces [Figs. 3, S1(g), S5(g)]. Alteration of the termination types can be understood in terms of strain-composition coupling at the interfaces [38]. In the thinner films, preservation of the tensile substrate strain [29] leads to smaller *c*-domain tetragonality ($c/a \approx 1.048$), which favors the incorporation of Sr into PZT and thus the SrO-Zr/TiO_2 termination is maintained [Figs. 3, S1(g)]. While in the thicker films, the strain release results in larger *c*-domain tetragonality ($c/a \approx 1.063$), which favors the incorporation of Pb into $SrRuO_3$ and therefore gives rise to the RuO_2-PbO terminated interfaces [Fig. S5].

Similarly, the interface reconstruction, involving structural and strain mismatch, chemical diffusion and polarization discontinuity, leads to flexible polarization rotation at the RuO_2-PbO terminated interfaces in the thicker films [Figs. S5(d), S5(e)]. The rotation of the P_S orientation away from $[001]_T$ suggests that width of the PZT/$SrRuO_3$ interfaces are approximately 6 pseudocubic unit cells. Accordingly, presence of the interfacial CDWs can therefore be attributed to poorer screening of SrO-terminated $SrRuO_3$ [52], rather than to mismatch strain or strain release at the interfaces. This behavior is consistent with observations of interfacial CDWs near tensile-strained (x = 0.9) PZT/$SrRuO_3$ interfaces [Figs. 1c, S1(f)], compressive-strained (x = 0.6) PZT/$SrRuO_3$ interfaces [Fig. S9], and compressive-strained $BiFeO_3$/$SrRuO_3$ interfaces [Fig. S4], which are all terminated by SrO planes in the $SrRuO_3$ electrode. However, such interfacial CDWs are not observed near the RuO_2-PbO terminated PZT/$SrRuO_3$ interfaces.

With regard to the *a* domains in the DSO-substrated PZT thin films, reduction of the lattice tetragonality to $c/a \approx 1.00$ near the interface, as a result of compressive substrate strain (~

-4.57%) to the *c* axis, suggests that the polarization almost disappears there and the polarization screening at *a*-domain/$SrRuO_3$ interfaces does not need to be considered.

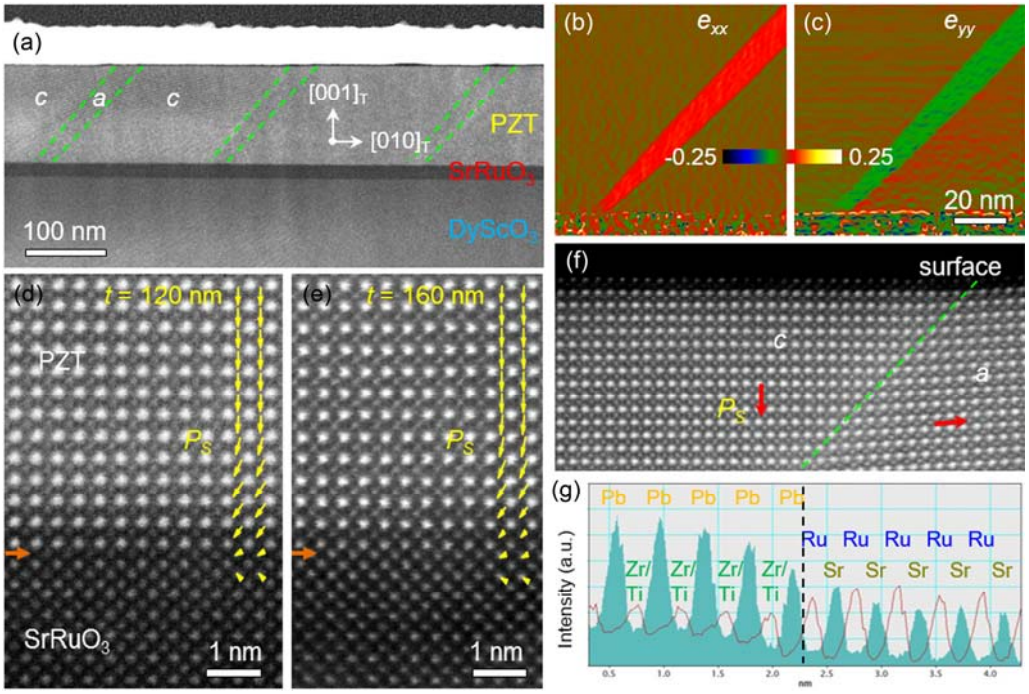

FIG. S5. (a) Representative HAADF-STEM image of a thicker (> 80 nm) (x = 0.9) PZT thin film recorded along $[100]_T$ direction. The green dash lines mark the 90° DWs. (b),(c) Strain maps of e_{xx} and e_{yy} obtained by using GPA. (d),(e) Atom-resolved HAADF-STEM images of PZT/$SrRuO_3$ interfaces in as-grown (d) 120 nm and (e) 160 nm thick films, with overlapping of the averaged polar displacement vectors ($\delta_{B\text{-}A}$). Orange arrows mark the RuO_2-PbO terminated interfaces. (f) Atom-resolved HAADF-STEM image showing a head-to-tail P_S orientation in ferroelastic domains near the surface. (g) Atom-column intensity profiles of proving the SrO-RuO_2-PbO-Zr/TiO_2 terminated interface (black dashed line) in a thicker PZT film.

6. Effect of interface termination of internal built-in field

Hysteresis loop measurements on the PZT (x = 0.9) thin films show the existence of internal built-in voltage (V_{bi}), which leads to evident shift of the PE loops along the voltage axis.

For thinner films with thickness t < 60 nm, a positive built-in voltage with V_{bi} = 0.55 V is identified [Fig. S6(a)]. As the film thickness increases to 60 nm < t < 100 nm, the built-in voltage becomes negligible with V_{bi} = 0.05 V [Fig. S6(b)]. As the film thickness t > 100 nm, the built-in voltage becomes negative with V_{bi} = -0.25 V [Fig. S6(c)]. As corroborated by our atomic-scale study (Figs. 1c, 3, S1g, S2, S5), the positive and negative built-in voltage is attributed to the SrO-Zr/TiO_2 and RuO_2-PbO termination, respectively. This is consistent with the result report on the system of $BiFeO_3$/(La,Sr)MnO_3 thin films [11]. For films with thickness at 60 nm < t < 100 nm, study on the (x = 0.9) PZT thin films has reported that the built-in field is dependent on the thermal treatment history, or density of oxygen vacancies on the film surfaces, which involve the density of 180° domains [39].

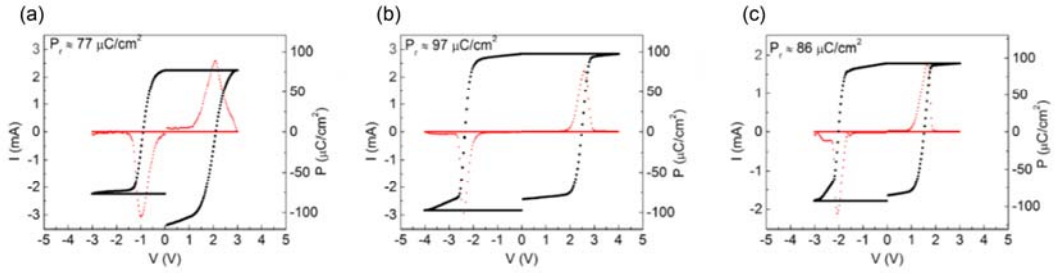

FIG. S6. Hysteresis curves showing the polarization (black curve) and the switching current (red curve) of PZT (x = 0.9) film. (a) Thin films with t < 60 nm, (b) intermediate films with 60 nm < t < 100 nm, (c) thick films with t > 100 nm (extracted from [31]).

7. Effect of oxygen pressure on polarization screening at PZT/$SrRuO_3$ interfaces

A study on ultrathin (3.5 ~10 nm) $PbTiO_3/SrRuO_3/SrTiO_3$ thin films has reported that, as a result of ionic compensation from surface species, the domain orientation can be changed with the oxygen partial pressure [40]. In our previous study, we have specially introduced oxygen vacancies into the (x = 0.9) PZT films by applying a post-annealing treatment to the ferroelectric

films at low (0.1 mbar) O_2 pressure. Changes of the DW conductivity corroborate that the oxygen vacancies had been successfully doped into the PZT films [Figs. S7(a), S7(b)] [29]. In order to examine the influence of oxygen partial pressure on interfacial polarization screening, the structural and polar displacement changes near the RuO_2-PbO terminated interfaces were investigated in the post-annealed films [Fig. S7(c)]. It is seen that the annealing treatment at low O_2 pressure does not alter the *c*-domain polarization orientation. By measuring positions of the atomic columns and calculating the poalr displacements [Fig. S7(d)], it is seen that along with magnitude reduction of P_S, the structural reconstruction also leads to flexible polarization rotation at the interface area. By comparison, it is seen that thickness of the monoclinically distorted interfacial unit cells (~ 7 unit cells) is about one unit-cell thicker than in the as-grown state (treated in 1 mbar O_2) [Fig. S5(c)].

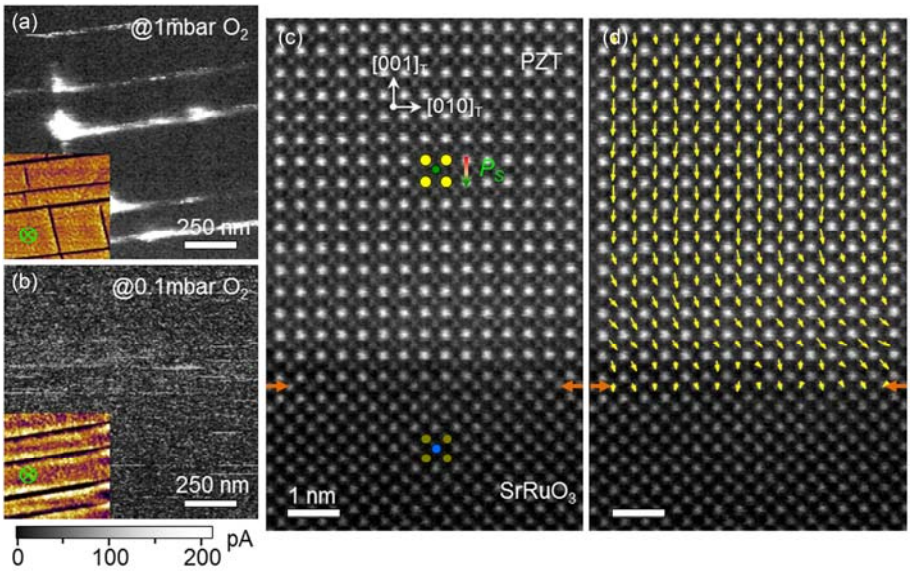

FIG. S7. (a),(b) Conductive atomic force microscopy (c-AFM) maps of 120-nm-thick (x = 0.9) PZT films treated at 300°C (2 h) in (a) 1 mbar and (b) 0.1 mbar O_2 atmospheres. The insets show piezoresponse force microscopy (PFM) amplitude images with the *c*-domain P_S pointing downwards (⊗, towards the PZT/$SrRuO_3$ interface). (c) Atom-resolved cross-sectional HAADF-

STEM image of the PZT sample annealed in a 0.1 mbar O_2 atmosphere. Orange arrows mark the RuO_2-PbO terminated interface. Atomic column types: Pb-yellow, Zr/Ti-green, Sr-dark yellow, Ru-blue. (d) P polar displacement vector ($\delta_{B\text{-}A}$) map overlapped onto the image of (c).

7. Flexible polarization rotation at metal (Au, Pt)/ferroelectric interfaces

In order to verify universality of the polarization screening mechanism, structural changes near the metal-electrode/PZT interfaces were investigated. Figure S9(a) shows an atomically-resolved TEM image of a Au/PZT (x = 0.9) interface in the 54-nm-thick PZT/$SrRuO_3$/$DyScO_3$ thin film, in which the Au layer had been sputtered onto the film before preparation of the FIB specimen. Although the outermost PZT unit cell is damaged as a result of Ar ion milling, the Au-PbO termination can be identified. By mapping positions of the atomic columns, the polar displacements ($\delta x_{O2\text{-}Zr/Ti}$) clearly reveal flexible polarization rotation near the Au/PZT interface, which has a width of ~ 3 unit cells, along with the damaged unit cell [Fig. S8(b)]. Lattice parameter measurements show that the *a* axis remains constant. However, the *c* axis gradually decreases as it approaches the interface, which facilitates conversion of the tetragonal phase into the monoclinic phase, especially within the 3 interfacial unit cells of PZT [Fig. S8(c)]. This behavior is consistent with magnitude reduction of polar displacements presented in Fig. S8(b). Similar structural changes are also observed at the Pt/PZT (x = 0.6) interface in the PZT/$SrRuO_3$/$SrTiO_3$ thin film, which is terminated by Pt-PbO atomic planes [Figs. 7S(d)-7S(f)]. In combination with our results from ferroelectric/oxide-electrode interfaces, our results demonstrate that the monoclinic-lattice-distortion-enabled flexible polarization rotation is a universal phenomenon at the ferroelectric-metal interfaces, which is the mechanism of screening ferroelectric polarization at such heterointerfaces.

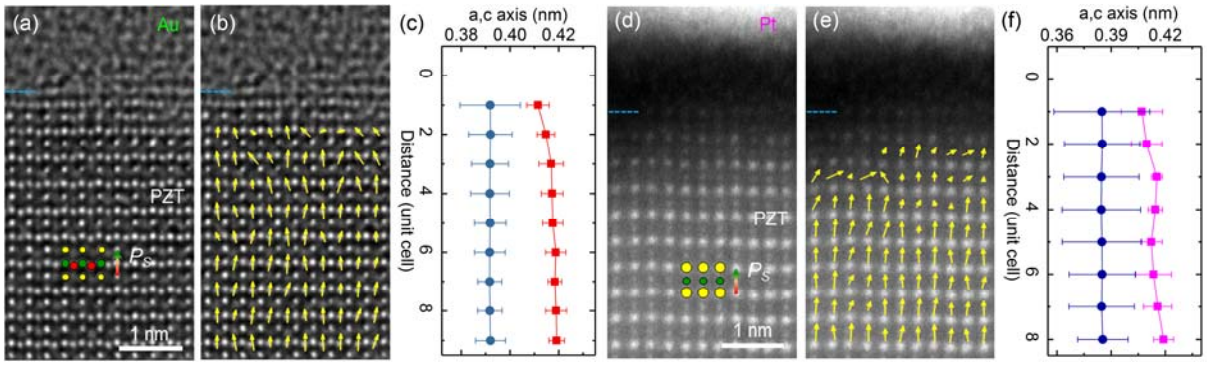

FIG. S8. (a) Atomically-resolved TEM image of a Au/PZT (x = 0.9) interface recorded along $[1\bar{1}0]_T$ direction under NCSI condition. (b) 2D polar displacement vectors ($\delta x_{O2\text{-}Zr/Ti}$) overlapped onto the image of (a). (c) Averaged lattice parameter changes plotted as a function of distance along the normal direction. (d) HAADF-STEM image of a Pt/PZT (x = 0.6) interface collected along $[1\bar{1}0]_T$ direction. (e) 2D polar displacement vectors ($\delta x_{Zr/Ti\text{-}Pb}$) overlapped onto the image of (d). (f) Averaged lattice parameter changes plotted as a function of distance along the normal direction. The blue dashed lines mark the Au/PZT and Pt/PZT interfaces.

8. Monoclinic lattice distortion and CDW at (x = 0.6) PZT/$SrRuO_3$ interfaces

In order to confirm that the ferroelectric-metal interfaces may serve as seeds to nucleate new domains, mono-domain state (x = 0.6) PZT films grown on $SrTiO_3$ substrates were investigated in our *ex-situ* biasing experiments. Since the monoclinic phase is essentially featured by the in-plane polar displacements (e.g., $\delta x_{B\text{-}A}$), the electron probe was adjusted to scan the $[1\bar{1}0]_T$ orientated specimen along the *c*-axis direction, which is aimed to enhance the measurement accuracy of $\delta x_{B\text{-}A}$ and to minimize the influence of sample drift. Figure S9(a) shows an HAADF-STEM image of the PZT/$SrRuO_3$ interface at the initial state. As seen from the magnified image [Fig. S9(b)], the downward shifts of Zr/Ti columns show that the P_S in initial domains is oriented along the $[001]_T$ direction. While near the interface, the leftward shifts

of Zr/Ti columns clearly reveal that the monoclinic lattice distortion takes places at the ferroelectric-metal interface [Fig. S9(c)]. The measured lattice parameters indicate that the *a* axis is constant, while more pronounced changes are observed along the *c*-axis direction [Figure S9(d)], starting from the first interfacial unit cell of $SrRuO_3$. Up to the third unit cell on the PZT side, the *c* axis reaches its maximum, with c = 0.4246 nm (c/a = 1.099). The tetragonality then goes back to its normal value (c/a = 1.071).

Measurements of the atomic polar displacements further corroborate monoclinic lattice distortion at the interface [Fig. S9(e)]. Along the in-plane direction ($\delta x_{B\text{-}A}$), the displacement starts from the second unit cell of $SrRuO_3$ and disappears at the sixth unit cell of PZT, which reaches the maximum at the first two unit cells of PZT with $\delta x_{Zr/Ti\text{-}Pb} \approx 13$ pm. In other words, the width of the polarized interface is ~ 7 unit cells. Along the *c* axis direction, downward displacements of the Zr/Ti columns ($\delta z_{Zr/Ti\text{-}Pb} \approx$ -20 pm) in the PZT reverse its direction when approaching the first interfacial unit cell ($\delta z_{Zr/Ti\text{-}Pb} \approx 6$ pm). This displacement, which corresponds to a downward P_S orientation [Fig. S9(c)], penetrates into the $SrRuO_3$ electrode by 1 ~ 2 unit cells. As a result, associated with an enhancement of the *c* axis, the polarization forms a cycloidal ordering feature, as observed at the CDWs [Figs. 1(d), 4, S9(c)]. Here, width of "domain II" is only one unit cell thick. When compared with tensile-strained PZT films [Fig. S1(g)], the atom-column intensity profiles suggest that less Sr diffuses into the nearest-neighboring PbO plane [Fig. S9(f)]. This observation further suggests that the compressive substrate strain enhances the lattice tetragonality and P_S, and limits the incorporation of Sr into the PZT [38,46].

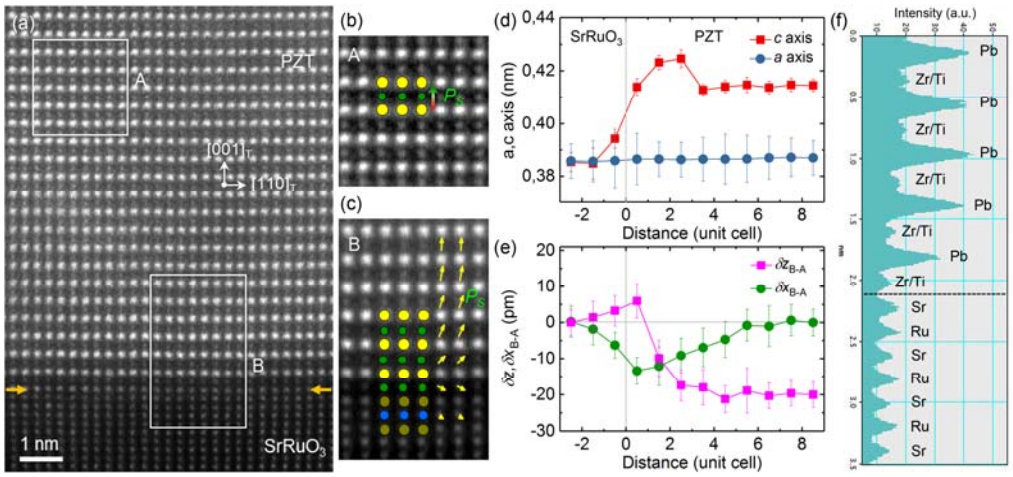

FIG. S9. Electron microscopy characterization of the initial domain state in $SrTiO_3$-substrated (x = 0.6) PZT/$SrRuO_3$ interface. (a) Atom-resolved HAADF-STEM image of a PZT/$SrRuO_3$ interface area recorded along $[1\bar{1}0]_T$ direction. Orange arrows mark the SrO-Zr/TiO_2 terminated interface. (b),(c) Magnified view of the A and B rectangular areas (filtered) indicated in (a), respectively. The averaged polar displacement vectors (yellow arrows) compiled from (e) are overlapped on the image. Atomic column types: Pb/O1-yellow, Zr/Ti-green, Sr/O1-dark yellow, Ru-blue. (d) Lattice parameters measured across the interface area. (e) The in-plane ($\delta x_{B\text{-}A}$) and out-of-plane ($\delta z_{B\text{-}A}$) displacements of B-site atoms plotted as a function of distance normal to the interface. (f) Atom-column intensity profile of evidencing the Pb-Zr/TiO_2-SrO-RuO_2 terminated interface (black dashed line).